



# Wide-frequency band measurement and analysis of electrochemical noise of Li/MnO<sub>2</sub> primary battery

E. A. Astafev<sup>1</sup>

Received: 27 December 2018 / Revised: 25 March 2019 / Accepted: 6 April 2019 / Published online: 23 April 2019  
© Springer-Verlag GmbH Germany, part of Springer Nature 2019

## Abstract

The electrochemical noise of a commercially produced Li/MnO<sub>2</sub> primary battery was measured during discharge via a constant value resistor. Power spectral density frequency dependences were calculated for different state of charge values across the frequency band from 0.02 to 5 kHz. It was shown that they possess close to linear frequency dependences. For high state of charge values, an intersection with the thermal noise spectrum was observed in a high-frequency band. The electrochemical impedance of the investigated type of battery was measured at different charge values both during discharge and following a relaxation pause. Impedance spectra obtained under load conditions were used to model the electrochemical noise spectra. It was shown that impedance parameters can be used to describe the electrochemical noise spectra in the frequency band above 500 Hz at state of charge values higher than 50%. Dependencies of electrochemical noise amplitude on discharge current value were investigated at different states of charge. It was shown that power spectral density has a linear dependency on discharge current at a power of about 2 for a charged battery and 2.5 for a discharged battery.

**Keywords** Electrochemical noise · Li-MnO<sub>2</sub> battery · Electrochemical impedance spectroscopy · Equivalent circuit analysis

## Introduction

The development of electrochemical power sources is one of the fastest growing areas in the field of modern electrochemical investigations. Consequently, new methods for their testing are also of great interest. Traditionally, various voltammetry, pulse, and impedance methods are used to estimate a state of health (SOH) and state of charge (SOC) values [1–5]. However, an alternative approach, widely used in the corrosion field [6–8], is that of electrochemical noise (ECN) measurement. Although this method has also been used for various electrochemical power sources [9–16], it has yet to find extensive application in this field.

One of the problems associated with this approach is that the ECN level of chemical power sources is very low and only appears under load conditions with a DC-current flow in the case of a fresh battery [17]. For this reason, specialised precision instrumentation is required [17–19]. Among electrochemical

power sources, a special place belongs to primary batteries [20–22]. Since these exhibit a relatively high ECN level [23–26], with significant noise behaviour changes having been observed for Li/SOCl<sub>2</sub> primary batteries during discharge [27], these electrochemical power sources represent a good choice for developing the ECN method. Li/MnO<sub>2</sub> batteries have not been so widely investigated as Li/SOCl<sub>2</sub> devices, with only a few publications extant [17, 25, 28]. However, no ECN spectrum modelling was made due to the lack of impedance spectra with DC-current flow measurement [20–22]. The analyses of ECN behaviour accomplished in works were mainly of a statistical character [28]. Therefore, in continuing the investigations started in works [17, 25], Robiton Li/MnO<sub>2</sub> batteries were chosen as objects of investigation in the present work in order to compare the results of using the ECN method to evaluate different types of electrochemical device.

An additional problem inherent to the ECN method is the difficulty of extracting information and the complexity of processing the data. Different approaches for overcoming these problems include spectral analysis [15, 29–31], statistical calculations [14, 32], orthogonal expansion techniques [33–35] and flicker noise spectroscopy [36, 37]. The ground-breaking modelling of electrochemical systems carried out by V. A. Tyagai remains very relevant to this field [38]. In our opinion,

✉ E. A. Astafev  
tdsipch@list.ru

<sup>1</sup> Institute of Problems of Chemical Physics RAS, Acad. Semenov av. 1, Chemogolovka 142432, Russia

the spectral analysis of the ECN method based on a calculation of the power spectral density (PSD) frequency dependences is the most promising. With results comparable to electrochemical impedance spectra (EIS) data; moreover, successful attempts at modelling have already been carried out [26, 39].

Thus, the main aim of the current work was to measure the ECN of a commercial Li/MnO<sub>2</sub> primary battery during the process of discharge via a constant value resistor. The main data processing technique used was calculation of PSD frequency dependences. In an attempt to model the ECN spectra, EIS was used as a referee method. Statistical calculations as typically used for ECN data processing were additionally used to evaluate whether this method can be used to obtain useful information about the ECN of the battery under test conditions [8, 14, 32, 40, 41].

The second aim of the work was to investigate the behaviour of the ECN of the battery under different DC-current values for different SOC values. We have already investigated the ECN dependency on DC-current value for a fuel cell [29, 30]. However, no such measurements have yet been performed for any type of the battery, since on the basis of existing publications, no ECN modelling attempts have been carried out for a Li/MnO<sub>2</sub> system [17, 25, 28].

## Experimental

Commercial Robiton CR2032 batteries were used as test objects. Their characteristics are as follows: capacity—200 mAh; voltage—3 V; maximum DC current—4 mA; 2032 package. Their compact size makes the shielding and the instrument connection easier.

The ECN measurements were carried out with the help of a NM-5-10K instrument (Electrochemical Instruments, Russia). This model was specially designed for ECN investigation of electrochemical power sources [18], which has already been successfully used as described in detail in several research works [17, 27]. The instrument was specially configured for the current work in order to conform with the impedance requirements of the objects under test.

The battery under test was connected to a high-pass, first-order filter. This consisted of a Panasonic (3300  $\mu\text{F} \times 16 \text{ V}$ , FM series, type EEUFM1C332L) low ESR electrolytic capacitor connected in parallel with a Murata GRM32ER60J107ME20L 100  $\mu\text{F}$  6.3 V ceramic capacitor and a Vishay MCU08050D2491BP 2.49 k $\Omega$  thin-film resistor having 0.1% precision and 25 ppm stability.

The main amplifier consisted of two Analog Devices ADA-4898-2 operational amplifiers connected in parallel for the ECN evolution during the investigation of continuous discharge. In this case, the gain of the amplifier was set to 530, while the instrument noise level was about 50  $\Omega$ . High-impedance

OPA2140 amplifiers were used with a gain of 114 in the case of ECN PSD on DC-current value investigation. These measurements were performed with the impedance of the battery under test quite high at a low SOC value. A low DC-current value results in a low observed ECN level. Thus, high-impedance, low-current-noise amplifiers were installed to eliminate the influence of input current noise of the amplifiers at high battery impedance [17, 27]. The voltage noise of the instrument is about 400  $\Omega$  at such a configuration; however, low ECN levels can be measured at higher than 100  $\Omega$  impedance of the object under test at the low-frequency band near 0.1 Hz.

An Analog Devices AD7177-2BRUZ 32-bit high-precision ADC was used to record the ECN. The same-type second ADC was used to measure the DC voltage and calculate the charge passed.

The load resistor was combined from two 1.2-k $\Omega$  resistors (C2-23, 2 W, 5%) connected serially to form an effective 2.4-k $\Omega$  resistor in continuous discharge experiments. Load currents were from 1.4 mA at the beginning of the discharge process to 0.7 mA at the end.

In order to investigate the ECN behaviour dependencies on discharging current value, 68-k $\Omega$  to 710- $\Omega$  load resistors were used for obtaining different DC-current values. These resistor values resulted in DC currents in the range from 0.044 to 4.2 mA. This experiment was performed for four SOC values: 100%, 70%, 40%, 10%. Galvanostatic discharge at 2 mA for 30 h was performed to reach the next value of SOC. A pause of 10 h was taken following each galvanostatic discharge in order to let the battery equilibrate prior to the ECN measurement. For each SOC value, the DC-current scan was started from the lowest point in the ECN measurement. A lower value resistor was placed in each subsequent ECN measurement step to obtain a higher DC-current value. A 0.5-h pause was taken following each resistor connection in order to let the DC voltage and current stabilise. Following this, two spectra were measured, with their coincidence forming a criterion of accurate measurement.

A P-45X (Electrochemical Instruments, Russia) potentiostat-galvanostat equipped with a FRA-24M impedance measurement module was used for EIS measurements and galvanostatic discharge. Measurements were performed with AC amplitude of 5 mV in the potentiostatic regime in a frequency range from 500 kHz down to 0.02 Hz. The measurement performed with the relaxations included a 4-step sequence repeated for several times until the battery was discharged. These steps were as follows: galvanostatic discharge with 2 mA current for 7 h; relaxation for 3 h; potentiostatic DC-voltage held at the voltage value reached during the previous relaxation step; AC impedance. The measurement performed without relaxations consisted of two steps: galvanostatic discharge at DC-current of 1 mA for 7 h; AC impedance in potentiostatic regime at the DC-voltage value reached during the previous discharge step.

ECN PSD frequency dependences were calculated by means of Fourier transform. The ECN data was measured in two frequency bands with different ADC data rates—100 Hz and 10 kHz for each SOC value. Data arrays consisted of 30000 points, divided into 30 segments of 1000 points length each. A linear trend removal procedure was used after each [42]. The Fourier transform was applied individually to each segment and the obtained spectra were averaged for all 30 segments after this step. This processing technique had been successfully used in a number of our previous investigations [25–27]. Instrument noise was measured and processed in the same way and subtracted in a frequency domain. ECN PSD spectra were recalculated into equivalent noise resistance units with the use of Nyquist formula [43]. This step was performed to enable a comparison of the ECN data with the EIS data since the impedance real part spectrum represents the thermal noise level of the battery under test.

A 20th-order polynomial drift removal procedure followed by double moving average trend removal procedure by 400 points was applied to low-frequency data prior to the statistical analyses. High-frequency data were not considered in the statistical analysis due to the instrument noise level being relatively high across this frequency band but unable to be subtracted for skewness and kurtosis (high-order moments) data. Kurtosis data represented in the current work were not normalised by the  $-3$  value.

## Results and discussion

Figure 1 depicts the ECN evolution during the discharge process in the time domain. It can be seen that the ECN level increases slowly during the first 80% of the discharge process. A strong rise in the amplitude of fluctuations is observed for the final 20% of SOC. Low-frequency measurement results are shown. These were used in statistical data analyses in the current work.

EIS spectra are shown in Fig. 2. Figure 2a demonstrates the result corresponding to the measurement without relaxation

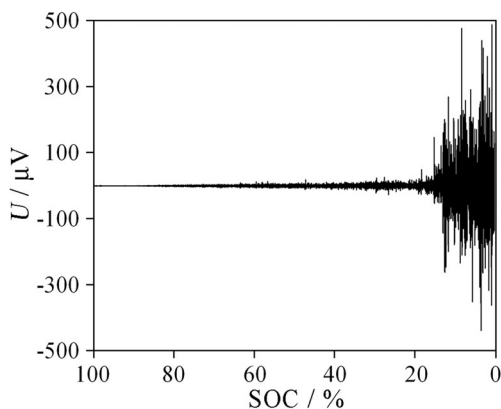


Fig. 1 ECN evolution shown in the time domain

pauses, while Figure 2b includes these pauses. It can be seen that all spectra possess an arc in the mid-frequency band. The diameter of this weakly depressed arc changes during the discharge process. However, these changes are much more pronounced in the case of the measurements with relaxations due to the arc diameter starting from the value of  $12 \Omega$  at 100% of SOC and reaching the value of  $520 \Omega$  at 30% of SOC. The diameter of the corresponding circle changes from  $12 \Omega$  at 92% of SOC to a maximum of  $52 \Omega$  at 40% of SOC in the case of measurements without relaxations. It is probably the case that this arc corresponds to the charge-transfer resistance. After the impedance measured under the DC current is exceeded, the electrochemical reaction speeds up and the charge-transfer resistance falls. On the other hand, when the DC-current passage is interrupted in the external circuit, the electrochemical reaction stops and only relaxation processes take place, leading to an increase in the charge-transfer resistance. The influence of the relaxation pause length on the behaviour of the EIS spectra was investigated for Li-ion batteries [44, 45].

Figure 3 shows the ECN PSD spectra for different SOC values. Figure 3b demonstrates a zoomed version of Fig. 3a. The level of ECN PSD frequency dependences increases during the discharge process. All spectra possess close to linear frequency dependences. Figure 4 demonstrates the example of the intersection of the ECN spectrum (curve 1) with the thermal noise spectrum (curve 3). It can be seen that the single slope of the spectrum breaks when the thermal noise level is reached at a certain frequency.

As it can be seen, each ECN PSD spectrum in Fig. 3 consists of three separate parts located in three frequency bands. The high-frequency spectrum corresponds to the high-speed measurement at the ADC sample rate of 10 kHz. The mid-frequency spectrum was calculated from the data measured at a sample rate of 100 Hz. The low-frequency spectrum was also calculated from the low-speed data, but here, a longer calculation segment was applied in order to extend the total spectra at low frequencies. It is well known that the PSD spectrum dispersion (which always looks noisy) decreases when averaging is increased but the low-frequency limit increases because the single data segment becomes shorter [46, 47]. Thus, we used a 1000-point segment length for the mid-frequency part of the spectrum calculation in order to keep its dispersion at the low level. However, we also decided to obtain the low-frequency data with higher dispersion due to having enlarged the segment length up to 10000 points. This made it possible to extend the low-frequency limit from 0.2 Hz down to 0.02 Hz and obtain acceptable total spectrum quality with the final frequency band wider than 5 orders.

Such an extension provided us with two important results. The first of these is that it is now possible to see that the low-frequency spectra possess a linear slope without any change at low frequencies. The second obtained result is that we were

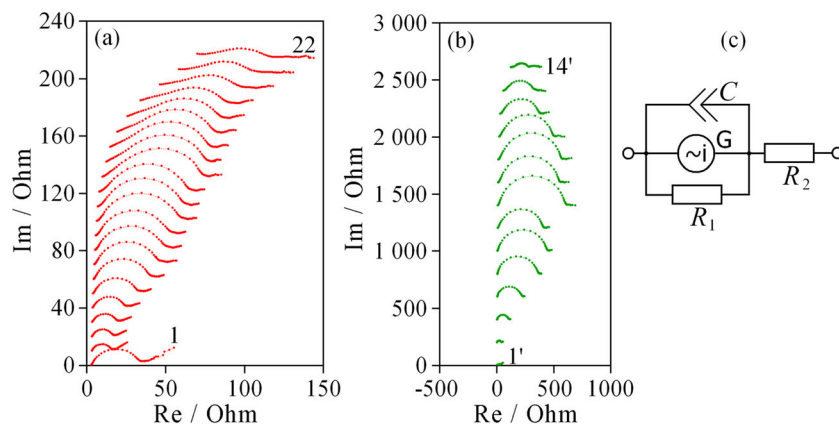


**Fig. 2** EIS data for the experiment with DC-current flow for different SOC values **(a)**: 1–4%, 22–88%; 4% of SOC increment between neighbouring spectra; curves are shifted by 10  $\Omega$  in a vertical direction for the better data representation. EIS data for the experiments with

relaxations **(b)**: 1–7%, 14–98%; 7% of SOC increment between neighbouring spectra; curves are shifted by 200  $\Omega$  in a vertical direction for the better data representation. ECN PSD RC-model **(c)**

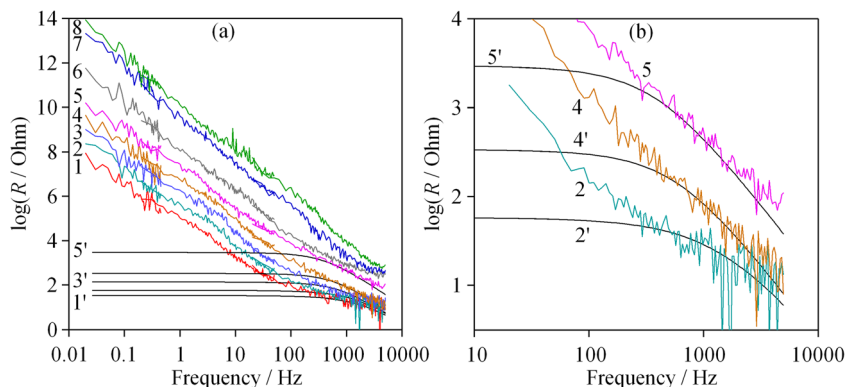
additionally able to test our calculations in this way. The segment length was changed from 1000 to 10000 points when the calculation of the mid-frequency part was completed and the low-frequency part had begun. Thus, the linear trend removal approximation interval was also increased by a factor of 10. It can be clearly seen that low-frequency and mid-frequency spectra overlap in several points for every SOC value, and that they coincide in this overlapping frequency band very clearly. Since the low-frequency part of each spectrum appears as an extension of the mid-frequency one, this means that the trend removal procedure eliminated only the part of the signal that needs to be removed for both calculations. If the trend removal procedure had been incorrect, these spectra would not coincide.

The low-frequency part of the ECN PSD spectrum possesses a single slope. We carried out a linear approximation in the frequency band from 0.02 up to 50 Hz. Corresponding results are shown in Fig. 5a. Two measurement results are shown by different colours as curves (1) and (2) to demonstrate the reproducibility of the experiment. It can be seen that no strong changes are observed for the first 70% of the discharge process. The slope value is close to  $-1.8$ . But the strong increase is observed for the final 25% of SOC, reaching the value

of  $-2.1$  for the discharged battery. This figure also demonstrates the fitting results obtained from EIS measurements.

Impedance spectra were fitted by the simplest RC circuit to obtain numeric parameters of the arc in the middle part of EIS spectra for all SOC values. The model of ECN PSD spectra is shown in Fig. 2c. This is equivalent to the simplest model developed by Tyagai [48], but with the pure capacitance replaced by a CPE element. The same circuit but without noise source generator G or resistor  $R_2$  was used for impedance mid-frequency part fitting. The values of charge-transfer resistance  $R_1$  and constant phase element (CPE)  $C$  as double-layer capacitance were calculated during the fitting procedure. CPE exponent values were also obtained since they define the high-frequency slope values of PSD frequency dependences in logarithmic coordinates. Their dependences on an SOC value are plotted as curves (3) and (4) in Fig. 5a in the form of slope values and multiplied by the value of 2. It can be seen that their behaviour correlates with changing ECN PSD spectrum slopes but that there are some numerical differences at SOC values lower than 50–30%. Curve (4) corresponds to the loaded EIS measurement. Physically, such conditions are much closer to those of the ECN measurement since both of them were carried out with a DC-current flow in the external circuit.

**Fig. 3** ECN PSD spectra for different SOC values: 1—90.5%, 2—83.6%, 3—78.8%, 4—71.4%, 5—54.4%, 6—7.9%, 7—5.2%, 8—2.9%. RC-modelling results 1'–5'. **a** All spectra shown. **b** High-frequency and low-PSD spectra





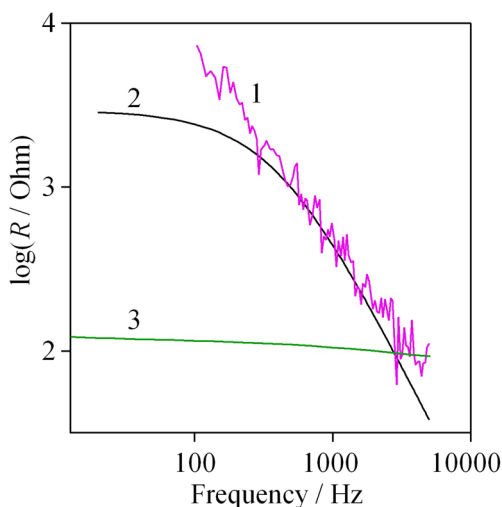


**Fig. 4** Example of ECN PSD spectrum—1 separation into modelling ECN spectrum—2, and thermal noise spectrum—3. 54.5% SOC value results are shown.

It is also interesting to note that curve (3) has a better numerical match with the ECN slope values. The fall of curve (4) begins at the SOC values close to those where the rise of curves (1) and (2) begins.

It seemed logical to try to use the model parameters to fit the ECN spectra for SOC values higher than 50%. The corresponding results of this attempt are shown in Fig. 3 as black curves (1')–(5'). Unfortunately, the time constants of  $R_1$ -C circuits turned out to be too short, leading to a situation in which only the high-frequency parts of the spectra could be successfully approximated. The results can be better seen on the scale of Fig. 3b. A reasonably good model approximation was obtained for the high-SOC curves (1)–(4).

Curve (5) (shown in pink) exhibits distortion at high frequencies. The reason for this is its intersection with the thermal noise level clearly shown in Fig. 4. In fact, this curve exhibits the best fitting result, since here, a clear intersection of the modelling result (curve 2 in Fig. 4, which represents high-frequency ECN itself) with the thermal noise curve 3, is observed. The measured ECN PSD spectrum (1) is directly coincident with the thermal noise curve 3 at the frequencies

located above the intersection point. Table 1 shows the modelling results in the form of the current PSD amplitudes of the noise generator. These values significantly exceed the shot noise level.

By taking a closer look at the ECN PSD spectra following the modelling attempt, it can be seen that low-SOC curves (6)–(8) in Fig. 3 exhibit distortion near the frequency of 100 Hz. The presence of small distortions in ECN PSD spectra can probably be explained by some secondary noise-generating process taking place in the low-frequency band. The second low-frequency generator starts to work due to the shunting of the high-frequency noise generator G by the charge-transfer resistance associated with it. Such a situation is in a good agreement with our previous results for a Li/SOCl<sub>2</sub> primary battery obtained over wide-frequency band measurements [27]. The ECN PSD spectra exhibit two slopes at low SOC values; moreover, the high-frequency part of spectra can be also modelled by EIS data [26]. It was also demonstrated in this work that a simple RC-model cannot be used to fit a low-frequency part of spectra for low SOC values. It seems logical to suppose that the high-frequency part of ECN spectra can be explained by the presence of the noise generator G associated with the charge-transfer resistance  $R_1$  for both battery types. Although the time constants are different for these electrochemical devices, this is to be expected considering that the tested batteries have different chemistry and geometry. Nevertheless, the situation with the low-frequency part of ECN spectra raises some questions about its nature.

Statistical analysis was performed next for the low-frequency data. Figure 5b demonstrates the standard deviation (SD) evolution during the discharge process. Considering that the low-frequency data trend removal included the double moving average by 400 points and the ADC sample rate was 100 Hz, this can be seen to correspond to the ECN behaviour at around 0.2–0.5 Hz.

Both curves demonstrate the same behaviour for the two separate measurements depicted in Fig. 5b. A small drop in amplitude is observed at SOC values higher than 80%; following this, a gradual increase takes place for the majority of

**Fig. 5** **a** ECN PSD slope absolute value evolution with the discharge process: 1—first experiment data, 2—second experiment data. Doubled CPE exponent values evolution obtained from EIS measurements: 3—with relaxations, 4—with the DC-current flow. **b** ECN standard deviation changing in the low-frequency band during the discharge process for two experiments

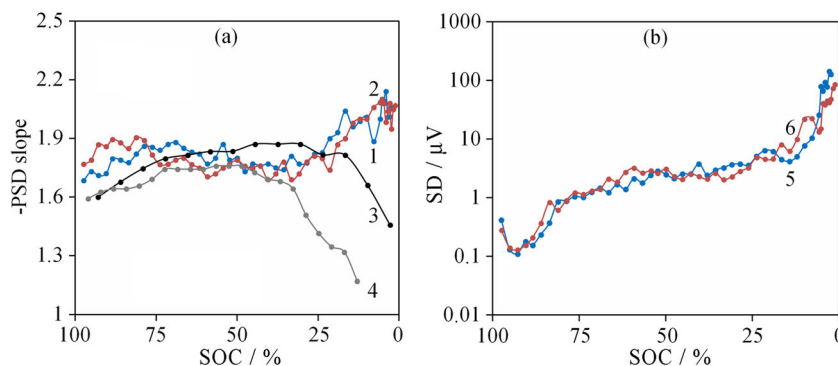


**Table 1** Current PSD amplitudes of modelling current noise generator for different SOC values (shot noise current PSD is  $21 \text{ pA}\cdot\text{Hz}^{-1/2}$  for the DC load current of  $1.4 \text{ mA}$ )

SOC, %	$I, \text{ nA}\cdot\text{Hz}^{-1/2}$
90.5	1.9
83.6	2.2
78.7	2.7
71.4	3.0
54.4	4.3

the subsequent discharge process. The increase in amplitude, observed for the final 20% of SOC, is in a good agreement with all previous spectral analysis results. It seems that the dependency of ECN parameters on SOC value shown in Fig. 5 cannot be used to precisely estimate SOC values of the battery of investigated type. However, ECN parameter values definitely can be applied as indicators for detecting the low-charge condition of the battery. The advantage of these indicators (PSD slope and SD value) is that their values change significantly during the last 20% of the battery discharge process but not after full discharge. Although 10–20% is a small reserve of the charge, it is a sufficiently accurate criterion on which to base a decision to replace the battery in the knowledge that it has been discharged by 80% or more. In critical applications, having such a reliable criterion can be very important.

Figure 6 demonstrates kurtosis and skewness evolution during the discharge process. Kurtosis values are not normalised to the  $-3$  value. It can be seen that both central moment values are near the standard noise values with a normal distribution for both shown measurement examples. A small increase in amplitude is observed for kurtosis values at high SOC values at the beginning of the discharge process. This is reflected in the fall of skewness to the value of  $-1.5$  when averaging the data from both experiments. Several peaks are observed for both central moments near 50% of SOC value. Some deviations from the standard values take place at the final 20% of discharge process where a small rise of kurtosis values is observed, and skewness starts to exceed the value of 0.5 and even 1 for the number of calculated SOC points. Such behaviour correlates with the previous results of Fig. 4, in which a rise in the ECN PSD slope values by an absolute

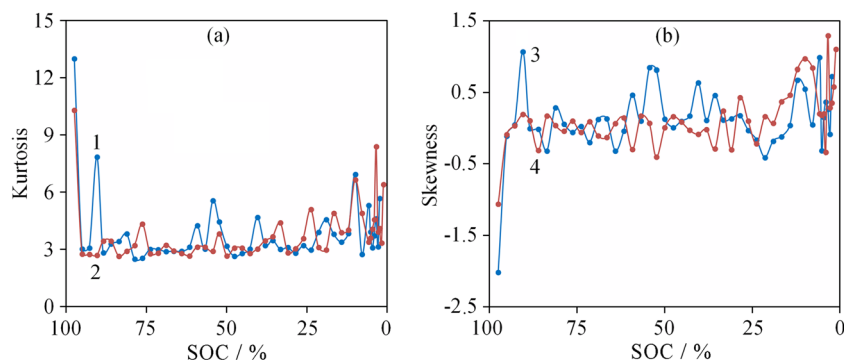
value is observed and an increase in the standard deviation values is exhibited in the final SOC values. Unfortunately, however, no further information can be obtained with the use of these calculations and there appears to be no possibility of modelling.

The second type of measurement was that of ECN PSD dependencies on a DC-current value. Figure 7 demonstrates ECN PSD spectra for different discharge current values for two SOC values given as examples (100% and 10%). As can be seen, each spectrum consists of two parts at different frequency bands. In this part of the investigations, there was no focus on sub-low frequency; rather, the aim was to obtain good precision. It was necessary to construct current PSD dependencies on a DC-current value as shown in Fig. 8 for all four SOC values investigated. Electrochemical impedance was measured for different DC-current values for all four SOC values in order to recalculate voltage PSDs into current PSDs.

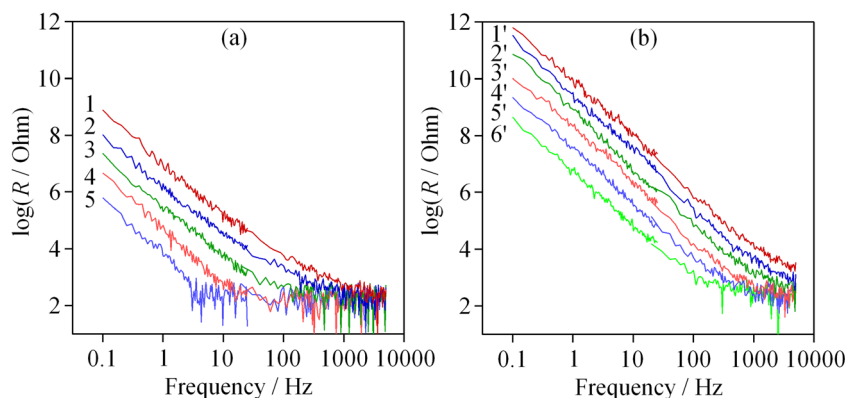
Figure 7 demonstrates that the ECN PSD maintains the linear frequency dependency when the discharging current is increased. The value of the slope stays almost unchanged when the discharging current is varied. However, the level of the ECN PSD spectrum gradually increases when the DC current is increased. As for the continuous discharge experiment of the previous type, the spectrum level increases with a decrease in SOC value when considering any DC-current value (vertical position changing of the spectrum with the same colour if moving from Fig. 7a to Fig. 7b). The low-level saturation of the spectra shown in Fig. 7 is due to the instrument noise level. This saturation, which starts from some given frequency and is prolonged at high frequencies, is wider for the low-level spectra.

Figure 8 demonstrates how low-frequency PSD values of ECN current (for two frequencies of 0.2 and 1.5 Hz) depend on the DC current. It can be seen that these dependencies can be linearly approximated for all SOC values. The slope of these dependencies gradually increases when the battery becomes more discharged from the value of about 2 for 100% of SOC to 2.5 for 10% of SOC. These slope values for PSDs in a voltage form are 1.95 for 100% and 2.00 for 70% of SOC. The slope value close to 2 is an attribute of impedance fluctuations. It is well-known from semiconductor noise measurements that

**Fig. 6** High-order moment evolution during the discharge process. **a** Kurtosis. **b** Skewness. Two experiments data are shown as curves (1) and (2) for both plots



**Fig. 7** ECN PSD spectra for different DC-current values: 1, 1'—4.2 mA; 2, 2'—2 mA; 3, 3'—1 mA; 4, 4'—0.3 mA; 5, 5'—0.13 mA; 6, 6'—0.044 mA. **a** 100% SOC. **b** 10% SOC



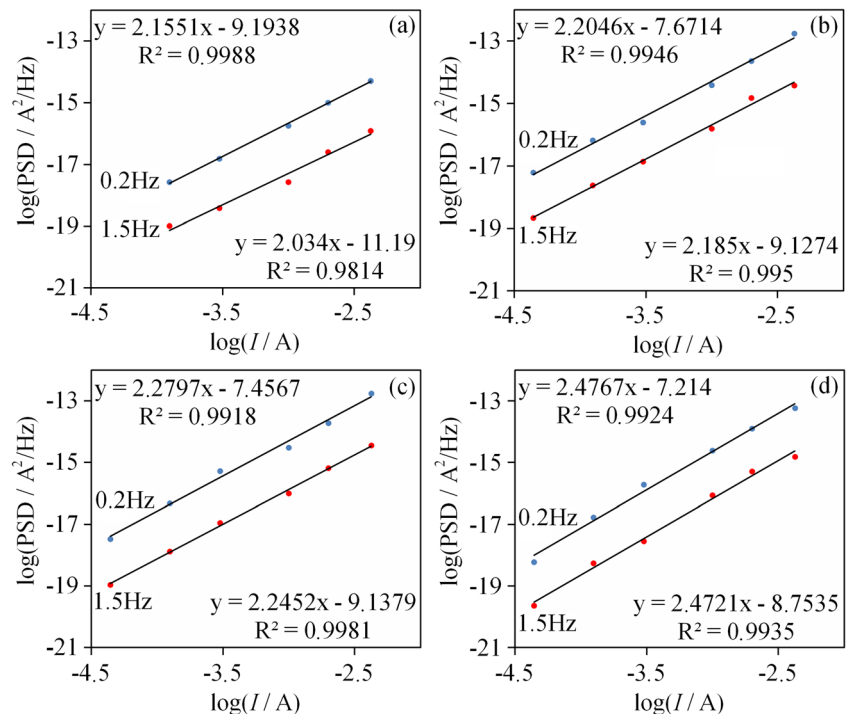
the dependency of PSD linear current on DC-current value in the power of 2 means that the conductivity fluctuation can explain observed noise if the PSD is in units of  $A^2/Hz$  [49]. In simple words, this proportionality is caused by the Ohms law. That means that the low-frequency part of the ECN PSD spectra can potentially be explained by the impedance fluctuations during battery discharge.

It is possible to summarise that ECN behaviour of the Li/MnO<sub>2</sub> primary battery of investigated type correlates with the behaviour of other chemical power sources [17, 25–27]. The amplitude of fluctuations tends to grow during the discharge process. The ECN PSD frequency dependence can be approximated by referring to several linear slopes depending on the SOC value as obtained for the Li/SOC<sub>1</sub> battery, which has also been investigated over a wide-frequency band [27]. The measurements limited by the frequency of 250 Hz of GP Li/MnO<sub>2</sub> primary batteries [25] did not show a change in the

high-frequency slope or achieve the thermal noise level due to limitations of the instrument used (in terms of the ADC data rate and instrument noise level). The ECN PSD slope changes were strong for a GP battery utilised in work [25] at the last part of discharge process too, as for the Robiton model investigated in the current work.

Based on the results of the present work and our previous investigations [17, 25–27], it is possible to say that the high-frequency part of the ECN PSD spectra coincides with the thermal noise frequency dependence starting from a frequency of 1 kHz or higher depending on the SOC value. The linear slope is observed in the frequency band from 0.1–500 Hz up to the frequency of intersection with thermal noise spectrum depending on the battery type, as well as its chemistry and SOC value. This slope behaviour can be described by the simple RC model constructed from a CPE of double-layer capacitance and a charge-transfer resistance having a white

**Fig. 8** Current ECN PSD values dependency on DC-current value for two frequencies and different SOC values. **a** 100%. **b** 70%. **c** 40%. **d** 10%



noise generator associated with it. The low-frequency band ECN data also possesses a linear slope. Here, the situation is similar even for those fuel cells where high-frequency noise can also be associated with the charge-transfer [29, 30]. The only difference is that a low-frequency plateau can be reached due to the capability of a fuel cell to work under steady-state conditions for a long time (over a week) in contrast to a battery [16]. More complex measurements, analyses and modelling are required to explain the phenomena for both batteries and fuel cells. It is most likely that only non-electrochemical methods of investigations [50–53] can help to directly find out the nature of the ECN in the low-frequency band because EIS and ECN methods provide quite relative information [54]. The only explanation for this is that it is caused by oscillations of low-frequency impedance components. This is derived from the ECN PSD dependencies on DC-current value demonstrated in the current work and agrees with the suggestions made in works [55] considering the low-frequency noise of fuel cell. But Schottky noise [56] cannot be used as a main ECN source.

## Conclusions

The electrochemical noise of a primary Li/MnO<sub>2</sub> battery was measured across a wide-frequency band during the discharge process. A significant increase in the ECN amplitude and PSD spectra levels was observed during the last 20–25% of the discharge process. A gradual increase in the noise amplitude can be observed for the higher SOC values.

For the first time, EIS data were obtained under DC-current flow conditions and compared to those values measured following relaxations for the different SOC values of the primary Li/MnO<sub>2</sub> battery. Significant differences were observed between these two measurements. The loaded measurement spectra were fitted with the simple RC model. Double-layer CPE and charge-transfer resistance values were used as the primary parameters for modelling the ECN PSD frequency dependences of the Li/MnO<sub>2</sub> battery. This modelling attempt was successful in the high-frequency band within the range of SOC values higher than 50%. Thus, a strong connection between ECN and IES spectra was demonstrated for the battery using the basic approaches developed by Tyagai for model electrochemical systems.

Statistical analysis has shown that standard deviation values correlate with the ECN PSD spectra parameters such as slope value and amplitude. Since the majority of changes in these parameters take place during the last 20% of the discharge process, they can be applied as indicators for the detection of the low-charge condition of batteries used in critical applications.

Current ECN PSD dependencies on DC-current value were constructed for a battery for the first time. These dependencies

show that current PSD depends linearly on DC current in the power of 2 at 100% of SOC and in the power of 2.5 at 10% of SOC. These values can be used to attribute low-frequency noise to the fluctuations of impedance of the battery during the discharge process.

**Funding information** This work was financially supported by the State Task of the Russian Federation (State Registration No. 01201361853).

## References

- Mingant R, Bernard J, Sauvant-Moynot V (2016) Novel state-of-health diagnostic method for Li-ion battery in service. *Appl Energy* 183:390–398
- Birkel CR, Roberts MR, McTurk E, Bruce PG, Howey DA (2017) Degradation diagnostics for lithium ion cells. *J Power Sources* 341: 373–386
- Farmann A, Waag W, Sauer DU (2015) Adaptive approach for on-board impedance parameters and voltage estimation of lithium-ion batteries in electric vehicles. *J Power Sources* 299:176–188
- Tant S, Rosini S, Thivel PX, Druart F, Rakotondrainibe A, Geneston T, Bultel Y (2014) An algorithm for diagnosis of proton exchange membrane fuel cells by electrochemical impedance spectroscopy. *Electrochim Acta* 135:368–379
- Hung MH, Lin CH, Lee LC, Wang CM (2014) State-of-charge and state-of-health estimation for lithium-ion batteries based on dynamic impedance technique. *J Power Sources* 268:861–873
- Bertocci U, Huet F (1995) Noise analysis applied to electrochemical systems. *Corrosion* 51:131–144
- Oltra R, Gabrielli C, Huet F, Keddam M (1986) Electrochemical investigation of locally depassivated iron – a comparison of various techniques. *Electrochim Acta* 31:1505–1511
- Homborg AM, Tinga T, van Westing EPM, Zhang Z, Ferrari GM, de Wit JHW, Mol JMC (2014) A critical appraisal of the interpretation of electrochemical noise for corrosion studies. *Corrosion* 70: 971–987
- Roberge P, Beaudoin R (1989) Voltage noise measurements on sealed lead-acid batteries. *J Power Sources* 27:177–186
- Baert DHJ, Vervaeke AAK (2003) Small bandwidth measurement of the noise voltage of batteries. *J Power Sources* 114:357–365
- Martinet S, Durand R, Ozil P, Leblanc P, Blanchard P (1999) Application of electrochemical noise analysis to the study of batteries: state-of-charge determination and overcharge detection. *J Power Sources* 83:93–99
- Huet F, Nogueira RP, Lailier P, Torcheux L (2006) Investigation of the high-frequency resistance of a lead-acid battery. *J Power Sources* 158:1012–1018
- Martemianov S, Adiutantov V, Evdokimov YK, Madier L, Maillard F, Thomas A (2015) New methodology of electrochemical noise analysis and applications for commercial Li-ion batteries. *J Solid State Electrochem* 19:2803–2810
- Martemianov S, Maillard F, Thomas A, Lagonotte P, Madier L (2016) Noise diagnosis of commercial Li-ion batteries using high-order moments. *Russ J Electrochem* 52:1122–1130
- Maizria R, Dib A, Thomas A, Martemianov S (2017) Proton exchange membrane fuel cell diagnosis by spectral characterization of the electrochemical noise. *J Power Sources* 342:553–561
- Astafev EA (2018) Frequency characteristics of hydrogen-air fuel cell electrochemical noise. *Fuel Cells* 18:755–762
- Astafev EA (2019) Electrochemical noise measurement methodologies of chemical power sources. *Instrum Sci Technol* 47:233–247. <https://doi.org/10.1080/10739149.2018.1521423>



18. Astafev EA (2019) The instrument for electrochemical noise measurement of chemical power sources. *Rev Sci Instrum* 90:025104–1–025104–7
19. Astafev EA, Ukshe AE (2019) Peculiarities of hardware for electrochemical noise measurement in chemical power sources. *IEEE Instrum Meas* <https://doi.org/10.1109/TIM.2018.2889232>
20. Manane Y, Yazami R (2017) Accurate state of charge assessment of lithium-manganese dioxide primary batteries. *J Power Sources* 359:422–426
21. Lee YG, Kim J, Kim S, Kim M (2010) 3.0V-class film-type lithium primary battery with highly improved energy density. *J Power Sources* 195:3715–3719
22. Krause FC, Jones JP, Jones SC, Pasalic J, Billings KJ, West WC, Smart MC, Bugga RV, Brandon EJ, Destephen M (2018) High specific energy lithium primary batteries as power sources for deep space exploration. *J Electrochem Soc* 165:A2312–A2320
23. Kanevskii LS (2009) Special features of discharge characteristics of different types of lithium-thionyl chloride cells and the problem of their diagnostics. *Russ J Electrochem* 45:835–846
24. Roberge PR, Halliop E, Famington MD (1991) Monitoring voltage fluctuations for the characterization of lithium cells. *J Power Sources* 34:233–241
25. Astafev EA, Ukshe AE, Dobrovolsky YA (2018) Measurement of electrochemical noise of a Li/MnO<sub>2</sub> primary lithium battery. *J Solid State Electrochem* 22:3597–3606
26. Astafev EA (2018) Electrochemical noise measurement of a Li/SOCl<sub>2</sub> primary battery. *J Solid State Electrochem* 22:3569–3577
27. Astafev EA (2019) Wide frequency band electrochemical noise measurement and analysis of a Li/SOCl<sub>2</sub> primary battery. *J Solid State Electrochem* 23:389–396
28. Uzundal CB, Ulgut B (2018) A method for voltage noise measurement and its application to primary batteries. *J Electrochem Soc* 165:A2557–A2562
29. Astafev EA, Ukshe AE, Gerasimova EV, Dobrovolsky YA, Manzhos RA (2018) Electrochemical noise of a hydrogen-air polymer electrolyte fuel cell operating at different loads. *J Solid State Electrochem* 22:1839–1849
30. Astafev EA (2018) Electrochemical noise measurement of polymer membrane fuel cell under load. *Russ J Electrochem* 54:554–560
31. Denisov ES, Evdokimov YK, Martemianov S, Thomas A, Adiantov N (2017) Electrochemical noise as a diagnostic tool for PEMFC. *Fuel Cells* 17:225–237
32. Maizia R, Dib A, Thomas A, Martemianov S (2017) Statistical short-time analysis of electrochemical noise generated within a proton exchange membrane fuel cell. *J Solid State Electrochem* 22:1649–1660
33. Grafov BM, Dobrovolskii YA, Davydov AD, Ukshe AE, Klyuev AL, Astafev EA (2015) Electrochemical noise diagnostics: analysis of algorithm of orthogonal expansions. *Russ J Electrochem* 51:503–507
34. Klyuev AL, Davydov AD, Grafov BM, Dobrovolskii YA, Ukshe AE, Astafev EA (2016) Electrochemical noise spectroscopy: method of secondary Chebyshev spectrum. *Russ J Electrochem* 52:1001–1005
35. Grafov BM, Klyuev AL, Davydov AD, Dobrovolskii YA, Ukshe AE, Astafev EA (2017) Median Chebyshev spectroscopy of electrochemical noise. *J Solid State Electrochem* 21:915–918
36. Timashev SF, Polyakov YS (2007) Review of Flicker noise spectroscopy in electrochemistry. *Fluct Noise Lett* 7:R15–R17
37. Astafev EA, Ukshe AE, Manzhos RA, Dobrovolsky YA, Lakeev SG, Timashev SF (2017) Flicker noise spectroscopy in the analysis of electrochemical noise of hydrogen-air PEM fuel cell during its degradation. *Int J Electrochem Sci* 12:1742–1754
38. Tyagai VA (1971) Faradic noise of complex electrochemical reactions. *Electrochim Acta* 16:1647–1654
39. Astafev EA, Ukshe AE, Dobrovolsky YA (2018) The model of electrochemical noise of a hydrogen-air fuel cell. *J Electrochem Soc* 165:F604–F612
40. Al-Mazeedi HAA, Cottis RA (2004) A practical evaluation of electrochemical noise parameters as indicators of corrosion type. *Electrochim Acta* 49:2787–2793
41. Reid S, Bell GEC, Edgemon GL (1998) The use of skewness, kurtosis and neural networks for determining corrosion mechanism from electrochemical noise data. In: *Corrosion*. NACE International, Houston, TX
42. Astafev EA, Ukshe AE, Leonova LS, Manzhos RA, Dobrovolsky YA (2018) Detrending and other features of data processing in the measurements of electrochemical noise. *Russ J Electrochem* 54:1117–1125
43. Nyquist H (1928) Thermal agitation of electric charge in conductors. *Phys Rev* 32:110–113
44. Kindermann FM, Noel A, Erhard SV, Jossen A (2015) Long-term equalization effects in Li-ion batteries due to local state of charge inhomogeneities and their impact on impedance measurements. *Electrochim Acta* 185:107–116
45. Schindler S, Bauer M, Petzl M, Danzer MA (2016) Voltage relaxation and impedance spectroscopy as in-operando methods for the detection of lithium plating on graphitic anodes in commercial lithium-ion cells. *J Power Sources* 304:170–180
46. Welch PD (1967) The use of fast Fourier transform for the estimation of power spectra: a method based on time averaging over short, modified periodograms. *IEEE Trans Audio Electroacoust* 15:70–73
47. Astafev EA (2018) Software and instrumentation methods of resolution enhancement in electrochemical noise measurement. *Russ J Electrochem* 54:1031–1044. <https://doi.org/10.1134/S0424857018130078>
48. Tyagai VA (1974) Noise in electrochemical systems. *Russ J Electrochem* 10:3–24
49. Bernamont J (1937) Fluctuations de Potential aux Bornes d'un Conducteur Metallique de Faible Volume Parcouru par un Courant. *Ann Phys* 11:71–140
50. Bowden W, Grey CP, Hackney S, Wanga F, Paik Y, Iltchev N, Sirotna R (2006) Lithiation of ramsdellite-pyrolusite MnO<sub>2</sub>; NMR, XRD, TEM and electrochemical investigation of the discharge mechanism. *J Power Sources* 153:265–273
51. Dose WM, Sharma N, Donne SW (2014) Discharge mechanism of the heat treated electrolytic manganese dioxide cathode in a primary Li/MnO<sub>2</sub> battery: an in-situ and ex-situ synchrotron X-ray diffraction study. *J Power Sources* 258:155–163
52. Shao-Horn Y, Hackney SA, Cornilsen BC (1997) Structural characterization of heat-treated electrolytic manganese dioxide and topotactic transformation of discharge products in the Li-MnO<sub>2</sub> cells. *J Electrochem Soc* 144:3147–3153
53. Buchberger I, Seidlmayer S, Pokharel A, Piana M, Hattendorff J, Kudejova P, Gilles R, Gasteigera HA (2015) Aging analysis of graphite/LiNi<sub>1/3</sub>Mn<sub>1/3</sub>Co<sub>1/3</sub>O<sub>2</sub> cells using XRD, PGAA, and AC impedance. *J Electrochem Soc* 162:A2737–A2746
54. Astafev EA (2018) Comparison of the method and hardware for electrochemical impedance with the method of electrochemical noise measurement and analysis. *Russ J Electrochem* 54:1022–1030. <https://doi.org/10.1134/S0424857018130066>
55. Denisov ES, Salakhova AS, Adiantov NA, Evdokimov YK (2017) Fluctuation-noise model for PEM fuel cell. *IOP Conf Ser Mater Sci Eng* 225:012110. <https://doi.org/10.1088/1757-899X/225/1/012110>
56. Schottky W (1918) Über spontane Stromschwankungen in verschiedenen Elektrizitätsleitern. *Ann Phys* 57:541–567

**Publisher's note** Springer Nature remains neutral with regard to jurisdictional claims in published maps and institutional affiliations.